Editors' Suggestion

Near-infrared hybrid quantum photonic interface for $^{171}Yb^{3+}$ solid-state qubits

Chun-Ju Wu,[1,2,3,4,†] Daniel Riedel,[1,†,‡] Andrei Ruskuc,[1,2,3] Ding Zhong,[1,2,3] Hyounghan Kwon,[1,3,§] and Andrei Faraon[1,2,3,*]

[1] *Thomas J. Watson, Sr., Laboratory of Applied Physics, California Institute of Technology, Pasadena, California, USA*

[2] *Institute for Quantum Information and Matter, California Institute of Technology, Pasadena, California, USA*

[3] *Kavli Nanoscience Institute, California Institute of Technology, Pasadena, California, USA*

[4] *Division of Physics, Mathematics and Astronomy, California Institute of Technology, Pasadena, California, USA*

(Received 12 December 2022; revised 18 July 2023; accepted 1 September 2023; published 6 October 2023)

$^{171}Yb^{3+}$ in YVO_4 is a promising candidate for building quantum networks with good optical addressability, excellent spin properties and a secondary nuclear-spin quantum register. However, the associated long optical lifetime necessitates coupling to optical resonators for faster emission of single photons and to facilitate control of single ^{171}Yb ions. Previously, single ^{171}Yb ions were addressed by coupling them to monolithic photonic crystal cavities fabricated via lengthy focused ion beam milling. Here, we design and fabricate a hybrid platform based on ions coupled to the evanescently decaying field of a GaAs photonic crystal cavity. For the most strongly coupled ion close to the GaAs-YVO interface, we find a 64-fold reduction in lifetime corresponding to a Purcell enhancement of 179. For an ion with a Purcell enhancement of 21, we experimentally detect and demonstrate coherent optical control. The results show a promising route toward a quantum network with ^{171}Yb-YVO_4 using a highly scalable platform that can readily be applied to other quantum emitters in the near-infrared.

DOI: 10.1103/PhysRevApplied.20.044018

I. INTRODUCTION

Transmitting quantum information and distributing entanglement through quantum networks are essential components in quantum technology and have applications in quantum communication and distributed quantum computing [1,2]. Building a scalable optical quantum network requires nodes with lifetime-limited optical transitions, efficient optical interfaces, long spin coherence times, high-fidelity spin and optical control, and multiqubit accessibility at each node. Among different platforms, optically addressable solid-state spin qubits are promising candidates due to the possibility of integration with nanofabricated devices leading to scalability [3,4]. Possible candidates include nitrogen vacancies [5,6], silicon vacancies [7,8], and tin vacancies [9,10] in diamond, color centers in SiC [11,12], defects in silicon [13], and rare-earth ions in crystals [14,15]. Rare-earth ions have been shown to possess long spin and optical coherence times in various hosts and will be the focus of this work [16,17].

Previously, we demonstrated that $^{171}Yb^{3+}$ ions inside YVO_4 have spin coherence times exceeding 10 ms, over 99.9% single-qubit gate fidelities, 95% post-selected optical readout and initialization fidelity, and additional nuclear spin qubit control, which are essential properties for building a quantum network [14,18]. In rare-earth ion platforms, coherent $4f$-$4f$ optical transitions are only weakly allowed inside crystals, therefore it is essential to couple ions to cavities with large quality factors and small mode volumes to increase the emission rate through Purcell enhancement. However, the nanofabrication of monolithic nanophotonic cavities from common rare-earth host materials is limited due to the unavailability of high-quality thin films and selective etching chemistries (aside from a few examples [19–21]). Here we demonstrate a near-infrared hybrid platform comprising a separately fabricated photonic crystal cavity that is subsequently transferred onto the host crystal [Fig. 1(a)] [22,23]. This platform possesses a smaller mode volume compared to Fabry-Perot microcavities [24,25], and, unlike the previous approach of focused ion beam milling [14,26], does not lead to crystal damage.

*Faraon@caltech.edu

†These authors contributed equally to this work.

‡Present address: AWS Center for Quantum Networking, Boston, Massachusetts, USA.

§Present address: Center for Quantum Information, Korea Institute of Science and Technology, Seoul, Republic of Korea.

Achieving significant enhancement in a hybrid photonic platform requires using a material with several important features. It needs to be transparent at the target wavelength, the refractive index needs to be significantly higher than the target crystal, and high-quality thin-film material should be readily available. The optical transition of $^{171}Yb^{3+}$-YVO_4 at 984.5 nm precludes the use of silicon. Hence, we choose GaAs as the photonic layer due to its transparency in the near- infrared, its large refractive index ($n_{YVO,c} = 2.17$, $n_{GaAs} = 3.52$) and the availability of wafer-scale thin films. High-quality-factor photonic crystal cavities have been fabricated at this wavelength using electron beam lithography, thus enabling mass production [27,28]. Recently, it has been demonstrated that the GaAs platform is amenable to scaling up deterministic solid-state photon-emitter interfaces [29]. In addition, wafer bonding techniques enable the creation of large-scale photonic integrated circuits [30]. In the following sections, we present the design and fabrication of these hybrid devices, and experimentally demonstrate optical control of single ^{171}Yb ions.

II. DEVICE DESIGN AND FABRICATION

Yb ions inside an a-cut YVO_4 crystal are coupled to a one-dimensional photonic crystal cavity with fundamental TE mode [31], where the electric field is mostly aligned with the c axis of the crystal. The photonic crystal design is based on unit cells with elliptical holes to engineer a band gap at 984.5 nm. A localized cavity mode is formed by quadratically tapering 20 central periods of a 44-period photonic crystal [Figs. 1(b) and 1(c)]. This is optimized to reduce radiation loss while maintaining a small mode volume. We engineer preferential cavity-waveguide coupling on one side by removing 11 mirror periods. The design of GaAs photonic crystal is chosen to enable high field penetration into YVO_4 without significantly decreasing the quality factor. We chose an effective index corresponding to the geometric mean of YVO and GaAs. Depending on the loss mechanisms a systematic study might yield better performance. Figures 1(b) and 1(c) show the simulated y-directed electric field (E_y) that will be aligned with the Yb optical dipole moment along the c axis, along with the pertinent cavity dimensions. The simulated squared electric field magnitude ($|E|^2$) at the YVO_4-GaAs interface is 40% of the maximum $|E|^2$ inside the GaAs layer. The effective mode volume is about $1.7(\lambda/n_{YVO_4})^3$ (normalized according to the strongest electric field in YVO_4 right at the surface) and the simulated radiatively limited quality factor is over 1×10^6. $|E_y|^2$ evanescently decays with distance from the interface, and the $1/e$ depth is 42 nm. To couple light from the cavity into a fiber, we utilize a fully etched grating coupler [32]. The grating coupler efficiency is optimized by modifying the grating dimensions leading to a simulated efficiency of about 25%.

Devices are fabricated on an epitaxial GaAs wafer using a standard electron-beam lithography procedure with an acceleration voltage of 100 kV (Raith EPBG 5000) [27]. A 500 nm positive-tone resist (ZEP) is patterned and subsequently developed using n-amyl acetate (ZED, Zeon

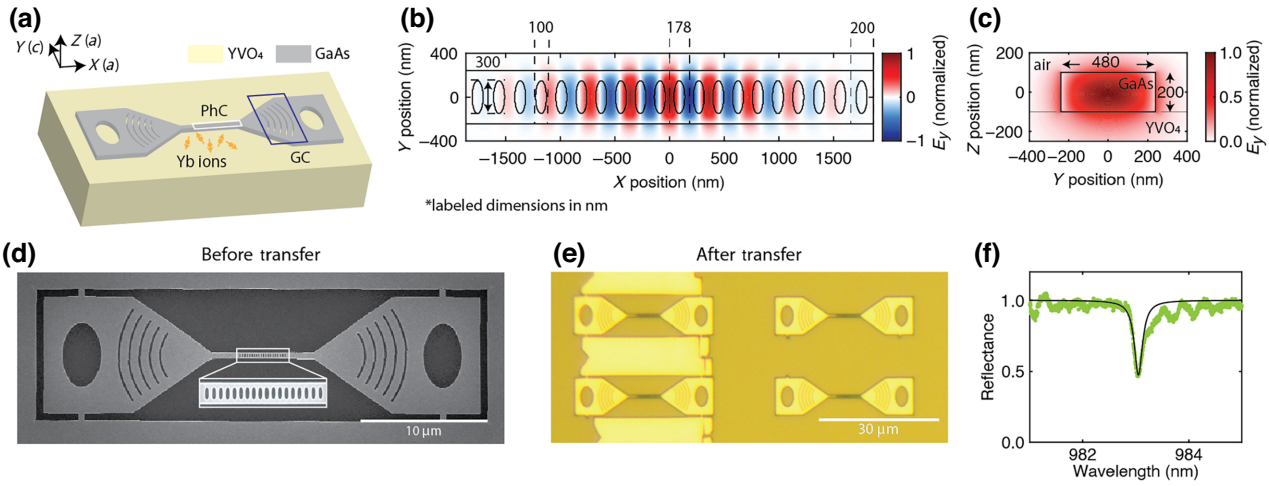

FIG. 1. Hybrid device platform for coupling to ^{171}Yb-YVO_4. (a) The device schematic. The GaAs photonic crystal cavity and YVO_4 crystal are shown in gray and yellow, respectively. Yb ions are shown with orange arrows and are located inside YVO_4. The crystal axes are shown next to the coordinate axes. The grating coupler (blue rectangle) is used for coupling light to a free-space setup. The photonic crystal cavity is indicated with a white rectangle. (b),(c) Simulated E_y field of the fundamental TE mode in the X-Y and Y-Z planes, respectively. Note the evanescent decay of electric field inside YVO_4. (d) Scanning electron microscope image of the suspended GaAs photonic crystal cavity before transferring onto YVO_4. (e) Optical image of the transferred device. The darker yellow substrate under the GaAs photonic crystal cavities is YVO_4. (f) Cavity reflection spectrum after transferring onto YVO_4. Data are shown in green dots and overlaid with a fitted black line, which gives a quality factor of 5300.

Corp.). The resist serves as the etch mask for an optimized inductively coupled plasma reactive-ion etcher with Cl_2-Ar chemistry. Devices are undercut by etching an $Al_{0.8}Ga_{0.2}As$ sacrificial layer in HF and cleaned subsequently using H_2O_2 and KOH to remove any residues [Fig. 1(d)]. Finally, suspended GaAs photonic crystal cavities are transferred onto the YVO_4 surface using a stamping technique [22]. Devices are aligned with the *a* axis and are perpendicular to the *c* axis. We use a polydimethylsiloxane stamp covered by a thin film of polycarbonate to pick up devices and subsequently release them onto YVO_4 using a transfer stage. The success rate of this procedure is over 90%. The YVO_4 crystal used in this experiment was polished from an undoped boule (Gamdan Optics) with an Yb concentration of 0.14 parts per million. The optical image after the transfer is shown in Fig. 1(e). The device used in these measurements has a quality factor of 5300 after transferring onto YVO_4 [Fig. 1(f)]. Typical quality factors of the devices before and after transfer are 15 000 and 5000, respectively, and are likely limited by the imperfect device fabrication and surface absorption [28].

III. DETECTION OF SINGLE YTTERBIUM IONS IN YVO_4

Experiments are performed in a Bluefors ^{3}He fridge (LD-He250) at 0.5 K and zero magnetic field. The experimental setup is depicted in Fig. 2(a), where acousto-optic modulated laser pulses are sent through a 99 : 1 beam splitter and focused onto the grating coupler through an aspheric lens doublet. The ion emission is sent back through the same fiber, and 99% of the light is directed to a superconducting nanowire single-photon detector. The light coupling is optimized using an *x*-*y*-*z* nanopositioner (Attocube), and the device resonance is tuned to the ion emission frequency through nitrogen condensation.

Figure 2(b) shows a resonant pulsed photoluminescence spectrum, where ion emission has been distinguished from the excitation in the time domain. The zero frequency offset corresponds to emission from Yb isotopes with no nuclear spin. At zero magnetic field, these isotopes contain degenerate Kramers doublets in both the ground and excited states [33]. The arrows indicate the ions used in this work.

To demonstrate single-ion addressability, a single-detector pulsed $g^2(t)$ measurement was performed on the ion indicated by the blue arrow [Fig. 2(c)]. The resulting $g^2(0)$ is 0.26 ± 0.09, lower than the two-ion limit of 0.5. The $g^2(t)$ measurement demonstrates a weak bunching feature, likely caused by spectral diffusion of the optical transition. By modeling spectral diffusion via rate equations, we derived and fitted the following function to the $g^2(t)$ data [34]:

$$g^{(2)}(t) = [1 + (\tau_w/\tau - 1)\exp(-|t|/\tau)] \times [1 - \exp(-(r + 1/\tau_{\text{ion}})|t|)], \quad (1)$$

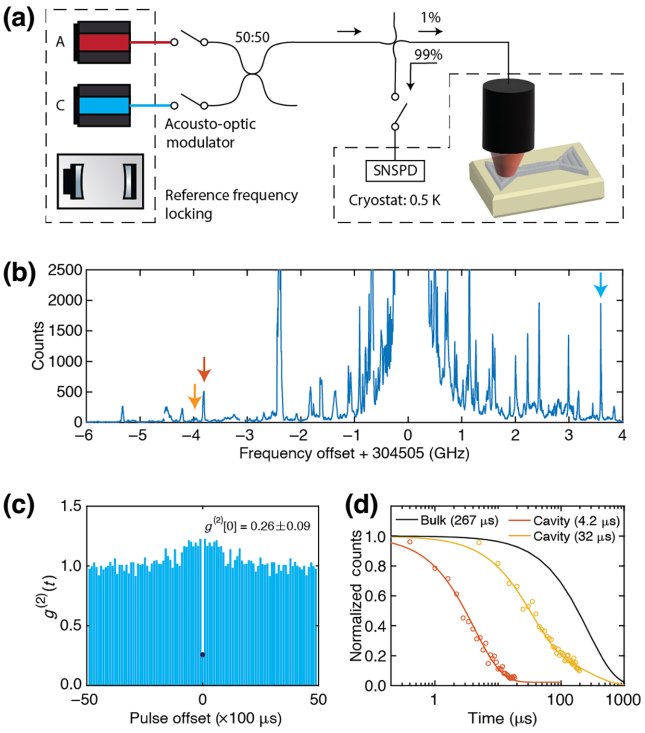

FIG. 2. Experimental setup and detection of single Yb ions. (a) Experimental setup. Optical pulses from two frequency locked lasers, labeled A and C according to the driven optical transition [Fig. 3(a)], are sent to the device located in a ^{3}He fridge at 0.5 K. Emitted photons are routed to a superconducting nanowire single-photon detector (SNSPD) in the same cryostat. Laser pulses are shaped using two double-pass acousto-optic modulators, and optical pulses are removed from the detection through time filtering and an acousto-optic modulator shutter setup. (b) Resonant photoluminescence spectrum. The large emission peak at 3 04 505 GHz corresponds to Yb isotopes with no nuclear spin. Isolated peaks inside the spectrum are mostly single Yb ions, the arrows indicate ions measured in subsequent experiments. Data was taken with 10 s integration time and 50 kHz repetition rate for each point. The fitted linewidth of red and blue ions are 27.3 MHz and 15.9 MHz, respectively.(c) Pulsed $g^{(2)}(t)$ measurement of the ion indicated with a blue arrow shows $g^{(2)}(0) = 0.26 \pm 0.09$. (d) Lifetime measured through time-resolved photoluminescence of ions indicated by red (4.2 ± 0.1 μs) and orange (32 ± 2 μs) arrows are shown with corresponding colors. Experimental data are shown with dots and overlaid with fitted exponential decays. The fit to the orange curve also includes an additional contribution from background bulk ions due to its lower intensity. Bulk lifetime is shown with a black line.

where τ is the spectral diffusion rate, τ_w is the rate of ion diffusion out of the detection window, r is the pumping rate, and τ_{ion} is the lifetime of the emitter [34]. We can derive a spectral diffusion correlation timescale of about 1 ms. The ion indicated by the red arrow has the shortest lifetime in this sample, measured to be 4.2 ± 0.1 μs [Fig. 2(d)]. This corresponds to a lifetime reduction of 64 times, which is consistent with the maximum lifetime

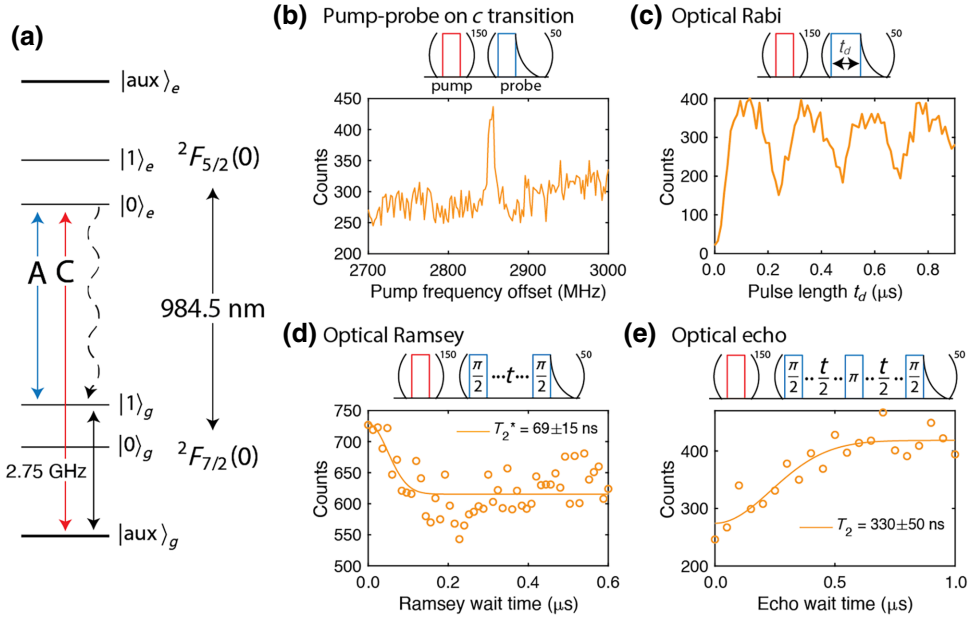

FIG. 3. Coherent optical control of a single ^{171}Yb ion. (a) Energy level structure of ^{171}Yb inside YVO_4 at zero magnetic field. Transition A (cavity enhanced) is shown in blue; transition C (non-enhanced) is shown in red. Cavity enhanced decay is shown with a dashed arrow. $|0\rangle_g$, $|1\rangle_g$, $|0\rangle_e$, $|1\rangle_e$ are magnetic field insensitive forming clock transitions. (b) Pump-probe measurement of the ^{171}Yb optical transitions. The pump frequency is varied around the C-transition with probe frequency fixed to the A-transition. In subsequent measurements, the ion is partially initialized by repeatedly pumping on this transition. The difference between the frequency noted in Fig. 3(a) and the measurement could be due to strain at the site of the ion. (c) Optical Rabi oscillation on the A-transition. (d) Optical Ramsey measurement on the A-transition gives $T_2^* = 69 \pm 15$ ns. (e) Optical echo measurement on the A-transition gives $T_2 = 330 \pm 50$ ns.

reduction ($\beta F_p = 83$) predicted by the Purcell effect [35]. $\beta = 0.35$ is the branching ratio of the transition [14] and $F_{p,\max} = (3/4\pi^2)(\lambda/n)^3(Q/V) = 237$. From the predicted maximum Purcell factor, measured lifetime, and the decay profile of the electric field strength given in Sec. II, we can derive maximum depths of the ions shown in Fig. 2(d), which are 12 nm and 101 nm for the red and orange ion, respectively.

IV. COHERENT OPTICAL CONTROL OF A SINGLE YTTERBIUM-171 ION

While Yb isotopes without nuclear spin show bright emission without initialization, they suffer from poor coherence times due to first-order susceptibility of transition frequencies to magnetic fields. Hereafter, we focus on ^{171}Yb ions which have an additional 1/2 nuclear spin giving a zero-field hyperfine energy-level structure shown in Fig. 3(a). These ions exhibit optical and spin clock transitions between the $|0\rangle_g$, $|1\rangle_g$, $|0\rangle_e$, and $|1\rangle_e$ levels, which are first-order insensitive to magnetic field noise, yielding enhanced coherence properties [14]. The A-transition has its dipole moment along the c axis of the crystal; it is copolarized with, and enhanced by, the cavity. Furthermore, it has no overlap with other Yb isotopes, making it suitable for optical readout. The C-transition has dipole moment perpendicular to the c axis of the crystal and is used for optical pumping and initialization.

To verify that the ion indicated by the orange arrow is ^{171}Yb [Fig. 2(b)], we performed a pump-probe measurement, where we varied the pump laser frequency and measured the photoluminescence on the A-transition. When the pump laser is resonant with the C-transition, the ion will be partially initialized into $|1\rangle_g$ and have brighter emission [Fig. 3(b)]. This initialization is performed prior to all subsequent measurements.

Resonant photoluminescence with varied excitation pulse length on the A-transition shows optical Rabi oscillation [Fig. 3(c)]. In this measurement, initialization is periodically applied after each sequence of 50 readout pulses. Combined with the limited cyclicity of the readout transition, this acts to saturate the photon counts and create a flat top feature. This ion has a lifetime of 32 ± 2 μs, leading to an A-transition cyclicity of 13 [14]. Characterization of the optical coherence properties is first performed with an optical Ramsey measurement, which includes two optical $\pi/2$ pulses with varied separation. We measured $T_2^* = 69 \pm 15$ ns corresponding to an effective linewidth of 4.6 MHz. The short-timescale optical frequency stability is measured using an echo consisting of an additional intermediate optical π pulse to rephase the coherence, yielding $T_2 = 330 \pm 50$ ns.

In these experiments, we were unable to perform optical coherence measurements for some of the ions that have shorter lifetimes. Ions in these hybrid devices with larger Purcell factors are closer to the surface and therefore more susceptible to surface defects. We postulate that the resulting charge noise could lead to excess spectral diffusion and deteriorated coherence properties. By contrast, in previously studied monolithic devices [14], well-coupled ions showed 1 μs postselected optical Ramsey and lifetime-limited optical echo (4 μs) coherence times since they were centrally located and farther from surfaces. The next step would be to characterize ion statistics with different Purcell factors and understand the limiting factor for the optical coherence in these hybrid devices.

V. CONCLUSION AND OUTLOOK

In this work, we fabricate suspended GaAs photonic crystal cavities and transfer them onto YVO_4 with a success rate of about 90%. We use a cavity with a quality factor of 5300 to address single ^{171}Yb ions, show a lifetime reduction of 64 times, and measure their optical coherence properties.

In the future, developing coherent microwave control of the spin transition will be essential. To improve the platform and increase count rates, refining fabrication of the photonic crystal cavity through surface passivation and further optimization of the lithographic procedure are crucial [28,36]. Switching to a shallow-etched grating coupler can also increase the waveguide to free-space coupling efficiency [37], and the overall photon collection rate into the waveguide can be improved by optimizing the cavity-waveguide coupling [38]. If the optical coherence is limited by surface proximity, we could dope Yb ions at different depths and characterize their properties. Optimizing the choice of the host crystal can also significantly improve the optical coherence [16,39]. Additional improvements could be attained by removing polishing-induced strain through plasma etching [40] and controlling the surface chemistry through systematic study of surface cleaning and preparation techniques [41]. Given the fabrication capability and the flexibility of the hybrid GaAs platform, combined with the excellent properties of ^{171}Yb-YVO_4, we think this approach is a promising route to build a quantum network.

ACKNOWLEDGMENTS

This work was funded by Office of Naval Research award no. N00014-19-1-2182, National Science Foundation Award No. 1936350, DOE-QIS program (DE-SC0019166), and Northrop Grumman. C.-J.W. acknowledges the support from a Taiwanese government scholarship. D.R. acknowledges support from the Swiss National Science Foundation (Project No. P2BSP2_181748). A.R. acknowledges the support from Eddleman Graduate Fellowship. D.R. contributed to this work prior to joining AWS. The device nanofabrication was performed in the Kavli Nanoscience Institute at the California Institute of Technology. We thank Joonhee Choi, Jake Rochman, Ioana Craiciu, Tian Xie, Mi Lei, Rikuto Fukumori, and Helena Guan for discussion, and Matt Shaw for help with superconducting photon detectors.

APPENDIX: DEVICE SIMULATION

Here we present more information about the device simulation. In the device, there are three different channels, κ_{scatter}, $\kappa_{\text{WG, trans}}$, and $\kappa_{\text{WG, refl}}$, that couple light out of the cavity, where κ_{scatter} is the scattering rate, and $\kappa_{\text{WG, trans}}$ and $\kappa_{\text{WG, refl}}$ are the rates of light coupling to the waveguide in the transmitted and reflected direction with respect to the incoming light. Our measurement configuration relies on photons that are coupling back to the reflected direction, therefore it is important that $\kappa_{\text{WG, refl}}$ is the dominant channel. In Fig. 4(a), we show how the designed quality factor is affected by the additional mirror number on both sides of the cavity. This shows that $\kappa_{\text{scatter}} = 1/Q_{\text{max}}$ only dominates at large mirror numbers in the simulation. In the experiment, we choose one side to have 12 mirror periods outside the tapered region, while the other side only has one, so that $\kappa_{\text{WG, refl}}$ is the dominant channel.

The driving of transitions with dipole moment along the crystal a axis is essential for initialization. One contribution to this drive comes from the input field that is perpendicular to the cavity mode (there is no TM band gap in our design). The other comes from a misalignment of the cavity mode field with respect to the crystal c axis. Figure 4(b) shows a histogram of the ratio of x- and y-directed electric field strengths of our mode [Fig. 1(a)]. The z direction is not shown because the electric field strength is negligible. For positions that have $|E_y| > 0.5|E_{y,\text{max}}|$, the median $|E_x|/|E_y| = 0.02$. These show that both the TM waveguide mode and the TE cavity mode can contribute to C-transition driving.

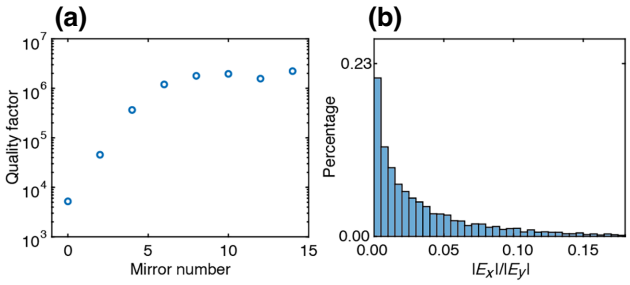

FIG. 4. Simulated device properties. (a) The simulated quality factor with different mirror numbers on both sides of the cavity. (b) Histogram of the x- and y-directed electric field strength ratio at positions with $|E_y| > 0.5|E_{y,\text{max}}|$.

[1] H. J. Kimble, The quantum internet, Nature (London) **453**, 1023 (2008).

[2] S. Wehner, D. Elkouss, and R. Hanson, Quantum internet: A vision for the road ahead, Science **362**, 9288 (2018).

[3] D. D. Awschalom, R. Hanson, J. Wrachtrup, and B. B. Zhou, Quantum technologies with optically interfaced solid-state spins, Nat. Photonics **12**, 516 (2018).

[4] G. Wolfowicz, F. J. Heremans, C. P. Anderson, S. Kanai, H. Seo, A. Gali, G. Galli, and D. D. Awschalom, Quantum guidelines for solid-state spin defects, Nat. Rev. Mater. **6**, 906 (2021).

[5] M. Pompili, S. L. N. Hermans, S. Baier, H. K. C. Beukers, P. C. Humphreys, R. N. Schouten, R. F. L. Vermeulen, M. J. Tiggelman, L. dos Santos Martins, B. Dirkse, S. Wehner, and R. Hanson, Realization of a multinode quantum network of remote solid-state qubits, Science **372**, 259 (2021).

[6] S. L. N. Hermans, M. Pompili, H. K. C. Beukers, S. Baier, J. Borregaard, and R. Hanson, Qubit teleportation between non-neighbouring nodes in a quantum network, Nature (London) **605**, 663 (2022).

[7] Z.-H. Zhang, P. Stevenson, G. m. H. Thiering, B. C. Rose, D. Huang, A. M. Edmonds, M. L. Markham, S. A. Lyon, A. Gali, and N. P. de Leon, Optically detected magnetic resonance in neutral silicon vacancy centers in diamond via bound exciton states, Phys. Rev. Lett. **125**, 237402 (2020).

[8] P.-J. Stas, Y. Q. Huan, B. Machielse, E. N. Knall, A. Suleymanzade, B. Pingault, M. Sutula, S. W. Ding, C. M. Knaut, D. R. Assumpcao, Y.-C. Wei, M. K. Bhaskar, R. Riedinger, D. D. Sukachev, H. Park, M. Lončar, D. S. Levonian, and M. D. Lukin, Robust multi-qubit quantum network node with integrated error detection, Science **378**, 557 (2022).

[9] A. E. Rugar, S. Aghaeimeibodi, D. Riedel, C. Dory, H. Lu, P. J. McQuade, Z.-X. Shen, N. A. Melosh, and J. Vučković, Quantum photonic interface for tin-vacancy centers in diamond, Phys. Rev. X **11**, 031021 (2021).

[10] R. Debroux, C. P. Michaels, C. M. Purser, N. Wan, M. E. Trusheim, J. Arjona Martínez, R. A. Parker, A. M. Stramma, K. C. Chen, L. de Santis, E. M. Alexeev, A. C. Ferrari, D. Englund, D. A. Gangloff, and M. Atatüre, Quantum control of the tin-vacancy spin qubit in diamond, Phys. Rev. X **11**, 041041 (2021).

[11] G. Wolfowicz, C. P. Anderson, B. Diler, O. G. Poluektov, F. J. Heremans, and D. D. Awschalom, Vanadium spin qubits as telecom quantum emitters in silicon carbide, Sci. Adv. **6**, eaaz1192 (2020).

[12] D. M. Lukin, M. A. Guidry, and J. Vučković, Integrated quantum photonics with silicon carbide: Challenges and prospects, PRX Quantum **1**, 020102 (2020).

[13] D. B. Higginbottom *et al.*, Optical observation of single spins in silicon, Nature (London) **607**, 266 (2022).

[14] J. M. Kindem, A. Ruskuc, J. G. Bartholomew, J. Rochman, Y. Q. Huan, and A. Faraon, Control and single-shot readout of an ion embedded in a nanophotonic cavity, Nature (London) **580**, 201 (2020).

[15] S. Chen, M. Raha, C. M. Phenicie, S. Ourari, and J. D. Thompson, Parallel single-shot measurement and coherent control of solid-state spins below the diffraction limit, Science **370**, 592 (2020).

[16] P. Stevenson, C. M. Phenicie, I. Gray, S. P. Horvath, S. Welinski, A. M. Ferrenti, A. Ferrier, P. Goldner, S. Das, R. Ramesh, R. J. Cava, N. P. de Leon, and J. D. Thompson, Erbium-implanted materials for quantum communication applications, Phys. Rev. B **105**, 224106 (2022).

[17] M. Zhong, M. P. Hedges, R. L. Ahlefeldt, J. G. Bartholomew, S. E. Beavan, S. M. Wittig, J. J. Longdell, and M. J. Sellars, Optically addressable nuclear spins in a solid with a six-hour coherence time, Nature (London) **517**, 177 (2015).

[18] A. Ruskuc, C.-J. Wu, J. Rochman, J. Choi, and A. Faraon, Nuclear spin-wave quantum register for a solid-state qubit, Nature (London) **602**, 408 (2022).

[19] S. Dutta, E. A. Goldschmidt, S. Barik, U. Saha, and E. Waks, Integrated Photonic Platform for Rare-Earth Ions in Thin Film Lithium Niobate, Nano Lett. **20**, 741 (2020).

[20] K. Xia, F. Sardi, C. Sauerzapf, T. Kornher, H.-W. Becker, Z. Kis, L. Kovacs, D. Dertli, J. Foglszinger, R. Kolesov, and J. Wrachtrup, Tunable microcavities coupled to rare-earth quantum emitters, Optica **9**, 445 (2022).

[21] A. Gritsch, L. Weiss, J. Früh, S. Rinner, and A. Reiserer, Narrow optical transitions in erbium-implanted silicon waveguides, Phys. Rev. X **12**, 041009 (2022).

[22] A. M. Dibos, M. Raha, C. M. Phenicie, and J. D. Thompson, Atomic source of single photons in the telecom band, Phys. Rev. Lett. **120**, 243601 (2018).

[23] D. Huang, A. Abulnaga, S. Welinski, M. Raha, J. D. Thompson, and N. P. de Leon, Hybrid III-V diamond photonic platform for quantum nodes based on neutral silicon vacancy centers in diamond, Opt. Express **29**, 9174 (2021).

[24] D. Riedel, I. Söllner, B. J. Shields, S. Starosielec, P. Appel, E. Neu, P. Maletinsky, and R. J. Warburton, Deterministic enhancement of coherent photon generation from a nitrogen-vacancy center in ultrapure diamond, Phys. Rev. X **7**, 031040 (2017).

[25] B. Merkel, A. Ulanowski, and A. Reiserer, Coherent and purcell-enhanced emission from erbium dopants in a cryogenic high-Q resonator, Phys. Rev. X **10**, 041025 (2020).

[26] T. Zhong, J. Rochman, J. M. Kindem, E. Miyazono, and A. Faraon, High quality factor nanophotonic resonators in bulk rare-earth doped crystals, Opt. Express **24**, 536 (2016).

[27] L. Midolo, T. Pregnolato, G. Kiršanskė, and S. Stobbe, Soft-mask fabrication of gallium arsenide nanomembranes for integrated quantum photonics, Nanotechnology **26**, 484002 (2015).

[28] K. Kuruma, Y. Ota, M. Kakuda, S. Iwamoto, and Y. Arakawa, Surface-passivated high-Q GaAs photonic crystal nanocavity with quantum dots, APL Photonics **5**, 046106 (2020).

[29] A. Tiranov, V. Angelopoulou, C. J. van Diepen, B. Schrinski, O. A. D. Sandberg, Y. Wang, L. Midolo, S. Scholz, A. D. Wieck, A. Ludwig, A. S. Sørensen, and P. Lodahl, Collective super- and subradiant dynamics between distant optical quantum emitters, Science **379**, 389 (2023).

[30] T. Komljenovic, D. Huang, P. Pintus, M. A. Tran, M. L. Davenport, and J. E. Bowers, Photonic Integrated Circuits Using Heterogeneous Integration on Silicon, Proc. IEEE **106**, 2246 (2018).

[31] Q. Quan and M. Loncar, Deterministic design of wavelength scale, ultra-high Q photonic crystal nanobeam cavities, Opt. Express **19**, 18529 (2011).

[32] E. Miyazono, I. Craiciu, A. Arbabi, T. Zhong, and A. Faraon, Coupling erbium dopants in yttrium orthosilicate to silicon photonic resonators and waveguides, Opt. Express **25**, 2863 (2017).

[33] J. M. Kindem, J. G. Bartholomew, P. J. T. Woodburn, T. Zhong, I. Craiciu, R. L. Cone, C. W. Thiel, and A. Faraon, Characterization of $^{171}Yb^{3+}$:YVO_4 for photonic quantum technologies, Phys. Rev. B **98**, 024404 (2018).

[34] G. Sallen, A. Tribu, T. Aichele, R. André, L. Besombes, C. Bougerol, M. Richard, S. Tatarenko, K. Kheng, and J. P. Poizat, Subnanosecond spectral diffusion measurement using photon correlation, Nat. Photonics **4**, 696 (2010).

[35] E. M. Purcell, Spontaneous emission probabilities at radio frequencies, Phys. Rev. **69**, 681 (1946).

[36] B. Guha, F. Marsault, F. Cadiz, L. Morgenroth, V. Ulin, V. Berkovitz, A. Lemaître, C. Gomez, A. Amo, S. Combrié, B. Gérard, G. Leo, and I. Favero, Surface-enhanced gallium arsenide photonic resonator with quality factor of 6×10^6, Optica **4**, 218 (2017).

[37] X. Zhou, I. Kulkova, T. Lund-Hansen, S. L. Hansen, P. Lodahl, and L. Midolo, High-efficiency shallow-etched grating on GaAs membranes for quantum photonic applications, Appl. Phys. Lett. **113**, 251103 (2018).

[38] E. N. Knall, C. M. Knaut, R. Bekenstein, D. R. Assumpcao, P. L. Stroganov, W. Gong, Y. Q. Huan, P.-J. Stas, B. Machielse, M. Chalupnik, D. Levonian, A. Suleymanzade, R. Riedinger, H. Park, M. Lončar, M. K. Bhaskar, and M. D. Lukin, Efficient source of shaped single photons based on an integrated diamond nanophotonic system, Phys. Rev. Lett. **129**, 053603 (2022).

[39] S. Ourari, Ł. Dusanowski, S. P. Horvath, M. T. Uysal, C. M. Phenicie, P. Stevenson, M. Raha, S. Chen, R. J. Cava, N. P. de Leon, and J. D. Thompson, Indistinguishable telecom band photons from a single erbium ion in the solid state, arXiv e-prints , arXiv:2301.03564 (2023).

[40] I. Friel, S. Clewes, H. Dhillon, N. Perkins, D. Twitchen, and G. Scarsbrook, Control of surface and bulk crystalline quality in single crystal diamond grown by chemical vapour deposition, Diam. Relat. Mater. **18**, 808 (2009).

[41] S. Sangtawesin, B. L. Dwyer, S. Srinivasan, J. J. Allred, L. V. H. Rodgers, K. De Greve, A. Stacey, N. Dontschuk, K. M. O'Donnell, D. Hu, D. A. Evans, C. Jaye, D. A. Fischer, M. L. Markham, D. J. Twitchen, H. Park, M. D. Lukin, and N. P. de Leon, Origins of Diamond Surface Noise Probed by Correlating Single-Spin Measurements with Surface Spectroscopy, Phys. Rev. X **9**, 031052 (2019).